Nonlinear effects in internal tide beams and mixing

Theo Gerkema, Chantal Staquet, Pascale Bouruet-Aubertot

To cite this version:

Theo Gerkema, Chantal Staquet, Pascale Bouruet-Aubertot. Nonlinear effects in internal tide beams and mixing. EGU (European Geophysical Union) General Assembly, Apr 2004, Nice, France. hal-00264977

HAL Id: hal-00264977
https://hal.science/hal-00264977v1

Submitted on 16 Aug 2021

Non-linear effects in internal-tide beams, and mixing

Theo Gerkema [a,*], Chantal Staquet [a], Pascale Bouruet-Aubertot [b]

[a] *LEGI, Grenoble, France*
[b] *LOCEAN/IPSL, Paris, France*

A non-linear non-hydrostatic model (MIT-gcm) is used to study the generation and propagation of internal tides. The model domain covers a continental slope and neighbouring parts of the deep ocean and shelf. Uniformity in the along-slope direction is assumed. We focus on the non-linear evolution of the internal tide once generated. In particular, we show that in the main region of generation, over the upper part of the slope, small-scale features occur, indicative of breaking and mixing. Far from the gener-ation region, non-linear processes are important in the reflection of the beam at the bottom, where higher harmonics are generated. This implies an energy transfer toward higher frequencies and the resulting shape of the energy spectra is consistent with observations. Turbulent and mixing processes are analysed by employing an adiabatic sorting method; thus, we calculate the development in time of the available poten-tial energy, the variation in the background potential energy due to irreversible processes, and the distribu-tion of the Cox number (the local turbulent diffusivity normalized by the background diffusivity) over the slope. With rotation, the transfer of energy to higher harmonics is reduced.

1. Introduction

In continuously stratified fluids, internal waves emitted from a localized source propagate as beams (e.g., Mowbray and Rarity, 1967; Turner, 1973). In the ocean, one of the dominant types

---

[*] Corresponding author. Present address: NIOZ, P.O. Box 59, 1790 AB Den Burg, Texel, The Netherlands.
E-mail address: gerk@nioz.nl (T. Gerkema).

of internal wave is the internal tide, formed by barotropic tidal flow over topography. Internal-tide beams, emanating from the upper part of the continental slope, have indeed been observed (Pingree and New, 1991; Jézéquel et al., 2002).

On the theoretical side, it is well-known that in an unbounded constantly stratified fluid, a monochromatic plane internal wave forms a solution of the non-linear Boussinesq equations (LeBlond and Mysak, 1978), because the contributions to the advective terms cancel; more generally, this is true for a monochromatic internal-wave beam (Tabaei and Akylas, 2003). The same may be supposed to hold in a bounded domain within the fluid interior, away from the boundaries; non-linear effects should be noticeable only sufficiently close to boundaries (topography, surface), or in regions of strongly varying stratification (such as the seasonal thermocline). In this paper we shall consider the first possibility.

One potential region for strong non-linear effects and mixing is the generation region itself, which lies at or just above the upper part of the slope. This is confirmed by in situ measurements made by Lien and Gregg (2001) in the upper part of an internal-tide beam, where an increased turbulent dissipation rate was found, indicative of non-linear effects and mixing. Of particular interest is the location where the slope is critical (i.e. the direction of the wave beam is tangent to the slope) and convex, which is usually the case at some position near the shelf-break. The barotropic tidal flow (which follows the slope) then has precisely the same direction as that of the particles in the beam, yielding optimal forcing. Moreover, barotropic currents are relatively strong near the shelf-break, which enhances the forcing too (this is borne out by the expression of the forcing term, as given e.g., by Baines (1982), where one finds an inverse proportionality with the square of local depth). This explains why one finds the main region of generation near the upper part of the slope.

Other potential regions for non-linear effects to occur are those where the beam reflects (bottom, surface), since here an in- and outgoing beam interact. Observations on the (first) bottom reflection of the internal-tide beam were made by Pingree and New (1991), although no specific analysis was made of the possible occurrence of non-linear effects.

In this paper we will employ the MIT-gcm (Marshall et al., 1997), a non-linear non-hydrostatic model that can (with a few adaptations) be used to study the generation and propagation of internal tides (Khatiwala, 2003; Legg, 2004). The usage of the model in its non-hydrostatic mode poses rather severe restrictions on the resolution, as the model's CPU rises considerably by adopting this mode. For this reason, we use the model here in a setting in which uniformity in the along-slope direction is assumed; notice that a velocity component in this direction can still be induced, by Coriolis effects. The basic settings and parameter choices are discussed in Section 2. In Section 3 we show the essential results of the calculations, and consider in detail the bottom-reflection of the internal-tide beam, and the non-linear effects involved. In Section 4 we turn to the generation region itself, and analyze small-scale features occurring over the slope. The analyzing method involves adiabatic sorting and allows one to calculate the available potential energy, and the Cox number (a measure of the local intensity of turbulent mixing). We show how the former develops in time, and how the latter is distributed over the slope. Results with and without Coriolis effects are discussed in Sections 3 and 4. Conclusions are presented in Section 5.

2. Model description

We employed the MIT-gcm to calculate the internal-tide fields, shown below. The MIT-gcm is described in detail in Marshall et al. (1997). The model is non-linear and non-hydrostatic, and the Boussinesq equations are solved with a finite-volume method in space and a second-order Adams–Bashforth scheme in time. We use the model here in an essentially 2D setting (i.e. we assume uniformity in the along-slope direction, while allowing for Coriolis effects).

The forcing, due to the barotropic tide, is added by prescribing the cross-slope barotropic flow at the boundaries, thus imposing a time-oscillatory but spatially constant barotropic flux. Furthermore, a sponge-layer is added at the lateral boundary of the deep ocean to absorb the baroclinic fields. In the model, the barotropic and baroclinic fields are not separated: the selective working of the sponge on the baroclinic fields is nonetheless attained by prescribing the friction as $\sim|u_x|u$. Due to the presence of the factor $|u_x|$, the sponge layer leaves the barotropic flow unaffected, as it is horizontally uniform in the sponge (the bottom being flat there). Finally, a KPP mixing-scheme (Large et al., 1994) was added to increase the diffusivity in regions where the Richardson number is small.

In the hydrostatic mode and for weak forcing, the model was tested against the linear hydrostatic internal-tide generation model developed and used by Gerkema (2002); the results were identical, except for minor features that are due to technical differences in the numerical schemes and methods.

In the experiments discussed below, the parameters were chosen as follows. The buoyancy frequency was taken constant: $N = 2 \times 10^{-3}$ rad/s; the tidal frequency (M2) $\sigma = 1.405 \times 10^{-4}$ rad/s. The Coriolis parameter was taken either zero (equator) or $f = 10^{-4}$ rad/s (mid-latitudes); we will refer to these cases as 'without' and 'with rotation', respectively. (In the case with rotation, we have changed the phase of the forcing to avoid the artificial creation of mean fields, as explained by Gerkema et al. (2004).) The depth of the deep ocean is 4 km, that of the continental shelf, 200 m. The length of the continental slope is 50 km; the slope is described by a cubic polynomial. Vertical diffusivity is 10^{-4} m^2/s, horizontal diffusivity 10^{-2} m^2/s; values of vertical and horizontal viscosity are equal to those of diffusivity, i.e. the Prandtl number is set to 1. This vertical diffusivity will later be referred to as "background diffusivity". In the calculations presented here diffusivity acts only on the temperature field, because salinity is taken constant throughout. The sponge-layer has a thickness of 50 km. No sponge was needed on the shelf, because the on-shelf propagating internal tides were weak, and their propagation slow (because of the shallowness), so that no significant reflection back into the domain occurred. The amplitude of the cross-slope barotropic flux is 100 m^2 s^{-1}. In the cross-slope direction 700 cells of 500 m are used, and in the vertical 160 of 25 m (in the deepest part), making the domain 350×4 km. The time step is 22.357 s, giving 2000 steps per tidal period (M2). Starting from a state of rest, runs span 15 tidal periods.

3. Main internal-tide beam and its higher harmonics

In the following figures, we leave out the first 50 km of the abyssal ocean (sponge-layer) as well as the last 50 km of the shelf (which hardly contains any signal at all). We will analyze the main internal-tide beam (frequency M2) and its harmonics (M4, M6 etc.). According to linear non-hydrostatic theory, the steepness γ of an internal-wave beam of frequency σ is given by

$$\gamma^2 = \frac{\sigma^2 - f^2}{N^2 - \sigma^2}, \tag{1}$$

(LeBlond and Mysak, 1978). By definition, the steepness γ is equal to $\tan\phi$, ϕ being the angle of the beam with the horizontal. Because $N > f$, γ is a monotonically increasing function of σ, implying that higher harmonics will be steeper.

3.1. Case without rotation

Fig. 1 shows the horizontal cross-slope current field at the end of the calculation. This is after exactly 15 tidal periods, a moment at which the barotropic currents are zero (to the extent that the barotropic signal behaves in a linear way, which we assume to be the case), so that the shown field represents solely the baroclinic signal. The most conspicuous feature in Fig. 1 is the (dark) internal-tide beam that originates from the upper part of the slope and travels diagonally into the deep ocean, where it reflects at the bottom ($x \approx 192$ km), then at the surface ($x \approx 137$ km), and later again at the bottom. From (1) we find for the angle of propagation: $\gamma = 0.070$ (recall that here $f = 0$). The numerical calculation gives $4/(192 - 137) = 0.073$, which deviates by less than 5% from the theoretical value of (1), derived from linear theory. As noticed above, linear theory can indeed be expected to work well in the interior of the domain (i.e. sufficiently far from the boundaries), for in an unbounded domain contributions to the jacobians cancel exactly for a monochromatic internal-wave beam.

We now consider the temperature field; Fig. 2a shows a snapshot, also after 15 tidal periods. Here too the main beam is visible, now in the vertical displacement of the isotherms. This is even more clearly seen in Fig. 2b, in which the initial temperature field (with horizontal isotherms) has been subtracted. Peak-to-trough amplitudes become as large as 250 m, which is in agreement with

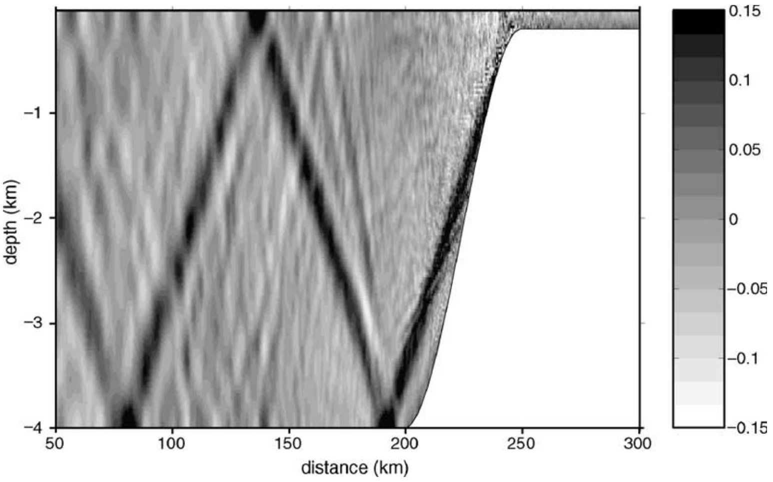

Fig. 1. The horizontal cross-slope baroclinic velocity component (in m/s), after 15 tidal periods.

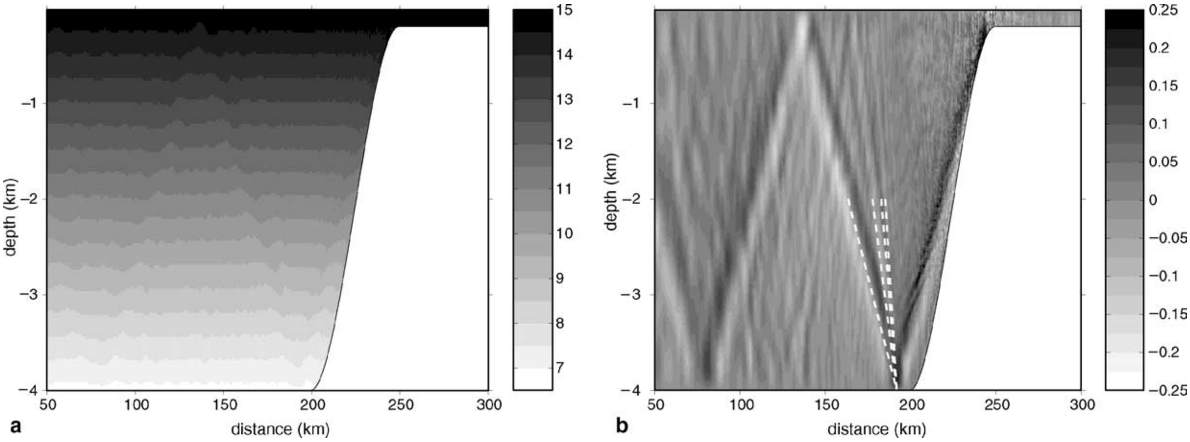

Fig. 2. (a) The temperature field (in °C), after 15 tidal periods. (b) The same, but now the initial (static) temperature field is subtracted (a temperature difference of 0.1 °C corresponds to a vertical displacement of 50 m). In (b) the theoretical steepness is indicated in dashed lines for M2, M4, M6 and M8 (from left to right).

the typical observed values for a similar strength in forcing (Pingree and New, 1991). One discerns also small-scale features near the upper part of the slope, which we shall consider in more detail in Section 4.

In both Figs. 1 and 2b one observes a clear weakening of the beam when one compares its intensity before and after the reflection at the bottom ($x = 192$ km). Concurrently, one sees thinner and steeper beams emanating from the region where the beam reflects. Using (1), one can easily check that these steeper beams are indeed higher harmonics. According to (1), the steepness of the first three higher harmonics (M4, M6 and M8) should be: $\gamma = 0.14$, 0.22, 0.29. From the data shown in Fig. 1 one finds: 0.14, 0.24, 0.33, which lie within 10% of the theoretical values. These two phenomena together show that the main beam loses energy by creating higher harmonics, a non-linear effect due to the interaction between the incoming and outcoming M2-beams. A similar result on the generation of higher harmonics has recently been found in numerical experiments on internal tides generated over a seamount in a deep ocean (Lamb, 2004), with a later theoretical analysis by Tabaei et al. (2005).

To get further insight into the generation of higher harmonics, we filtered the baroclinic current around M2, and its first harmonic M4, respectively. These signals are displayed at two "moorings", before and after reflection of the tidal beam (Fig. 3). Before reflection, the M4 component is very weak, less than 1% of the M2 component (compare frames a and b). By contrast, after reflection its amplitude is of the same order as that of the M2 component, being three times lower only (compare frames c and d). Its spatial structure is organized as a beam at depths between 1.5 and 3 km. Consistent with this, the amplitude of the M2 component is seen to be reduced after reflection (frame c).

Frequency spectra of the kinetic and available potential energy computed at the same two "moorings" are displayed in Fig. 4. These spectra are computed over the whole duration of the computation, namely 15 tidal periods, with a temporal sampling equal to 0.05 tidal periods. The kinetic and available potential energy levels coincide, as is confirmed in frames b and c, where the ratio between total kinetic energy and available potential energy is plotted versus frequency: this ratio is very close to 1 at all frequencies, in accordance with linear theory with $f = 0$. (We note

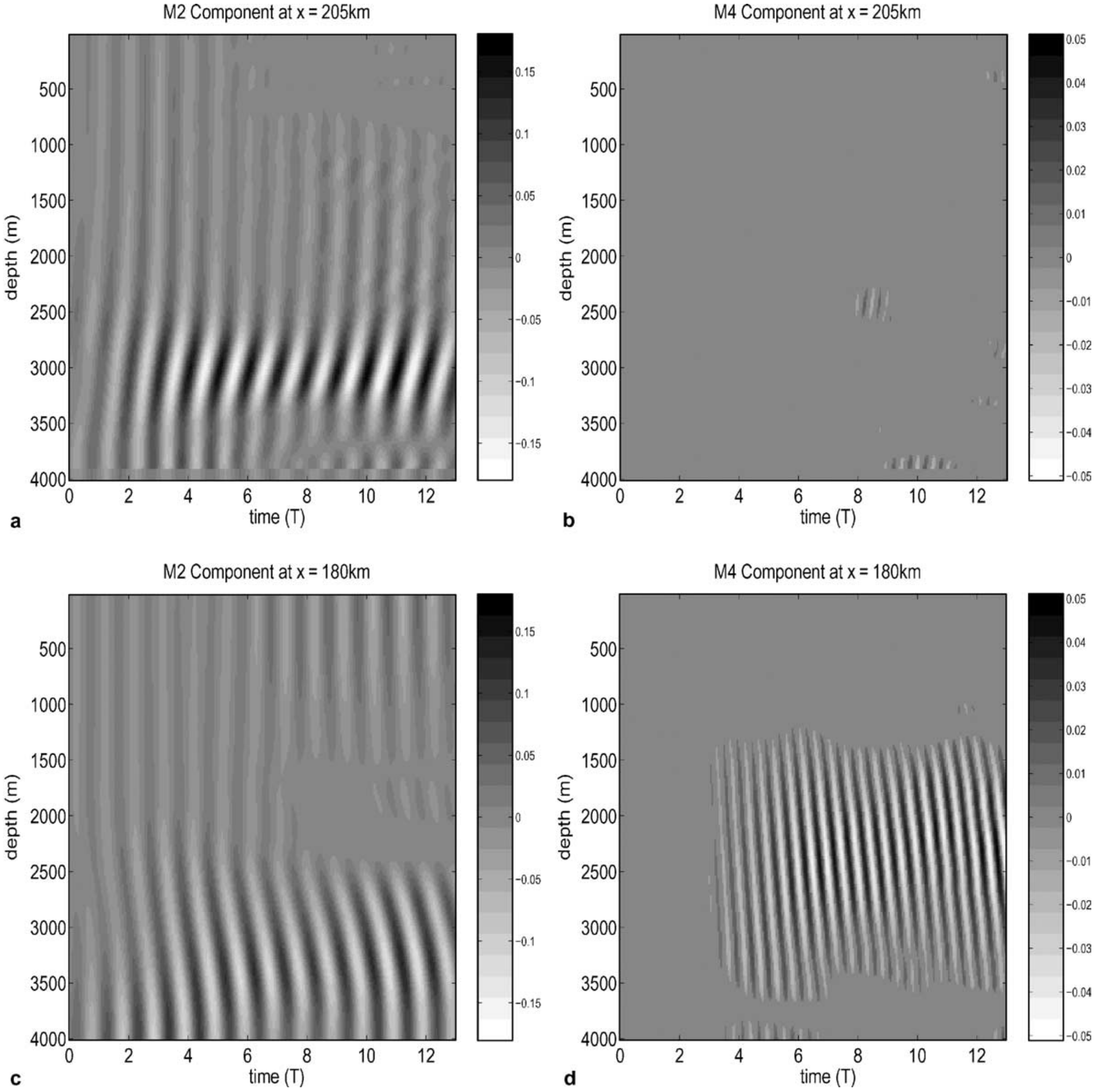

Fig. 3. Time-depth evolution (in tidal periods) of the filtered components of the baroclinic horizontal velocity (computed as the total field minus the depth average); panels a and b *before* reflection, c and d *after*, (a) M_2 at $x = 205$ km; (b) M_4 at $x = 205$ km; (c) M_2 at $x = 180$ km; (d) M_4 at $x = 180$ km.

that for non-linear waves the ratio can in principle be larger, because transfer of kinetic energy toward higher frequencies is restrained in two dimensions, see Bouruet-Aubertot et al., 1996.)

Comparison between the two moorings provides evidence of the reduced energy content of the M2 component after reflection and of the development of harmonics: M4, M6 and M8 are clearly visible. We estimated the energy transfer from the M2 internal tide to higher frequencies: about 5% is transferred to the first harmonic M4; this value is to be compared with a net energy decrease

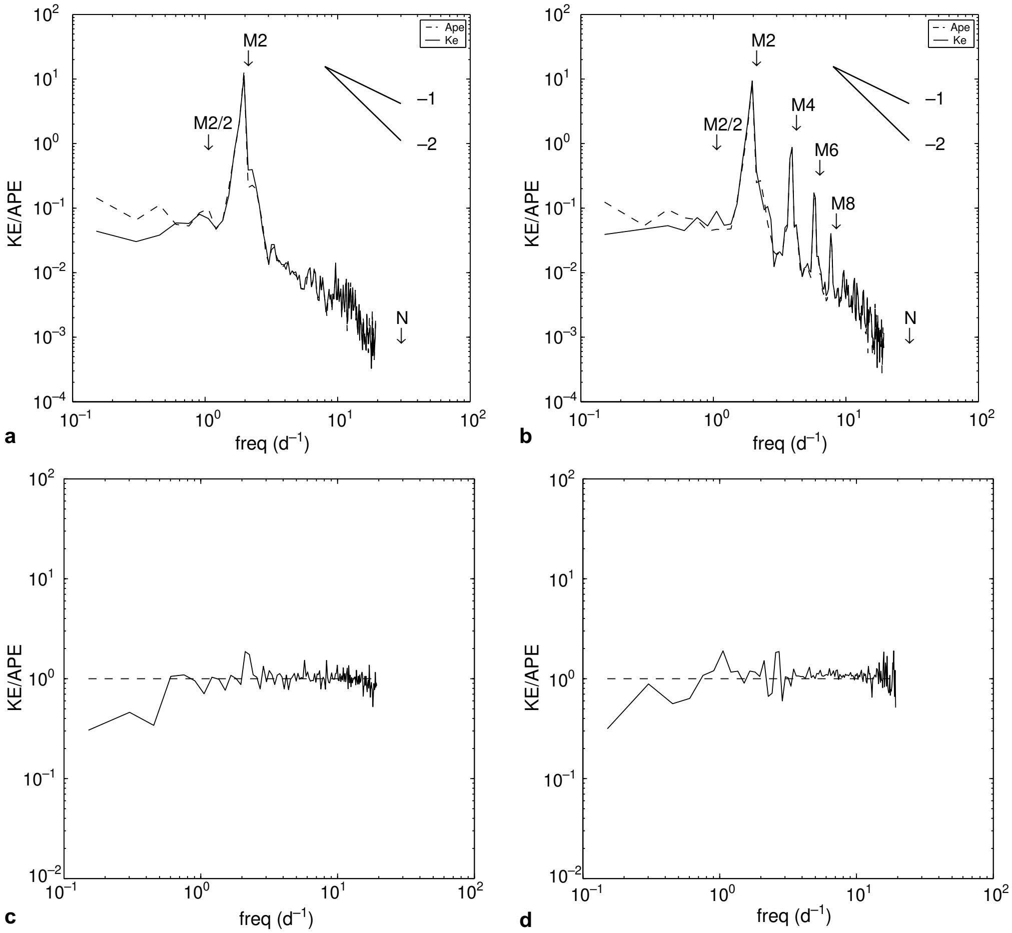

Fig. 4. Frequency spectra of kinetic and available potential energy, averaged over total depth, at two different "moorings", before and after reflection of the tidal beam: (a) at $x = 205$ km; (b) at $x = 180$ km; (c) ratio of total kinetic energy and available potential energy, as a function of frequency at $x = 205$ km; (d) the same ratio, but now at $x = 180$ km.

of the M2 component before and after reflection of about 16%. Transfers toward higher harmonics (M6, etc.) is less than 1%. We also find an increase in the energy content at other high frequencies (i.e. non-harmonics): from about 1% of the M2-energy before reflection to 4% after reflection. All in all, this means the M2 tide loses 7% (=16 − 5 − 1 − 3) of its energy to dissipation during reflection. We may thus say that, roughly, half of the loss of energy of the M2 beam can be ascribed to dissipation, and the other half to the transfer to higher frequencies.

3.2. Case with rotation

The inclusion of Coriolis effects gives a number of changes to the results shown above, and nearly all of them can be traced back to the dispersion relation (1). According to this expression,

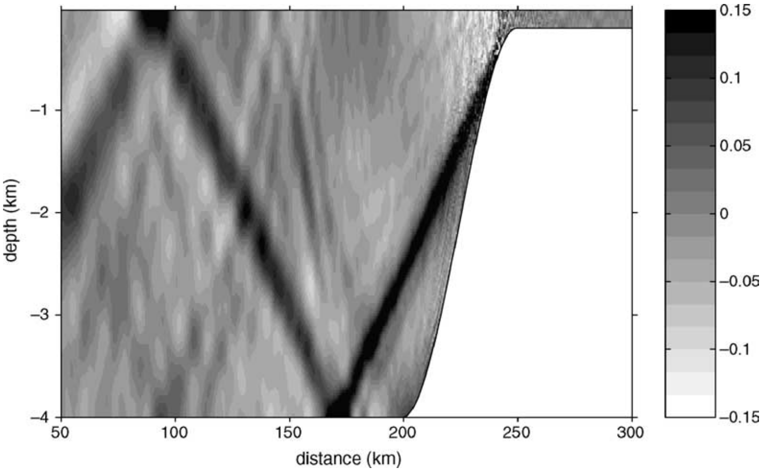

Fig. 5. Case with rotation. The horizontal cross-slope baroclinic velocity component (in m/s), after 15 tidal periods.

beams become less steep by including *f*, and this is indeed what we observe in Fig. 5. Higher harmonics are still visible, although less distinctly than in Fig. 1. From Fig. 5 we obtain the following estimates of the steepness of the M2, M4 and M6 beams: $\gamma = 0.052$, 0.14, 0.20, which are in satisfactory agreement with the theoretical values from (1): $\gamma = 0.050$, 0.13, 0.21. The M8 beam in this case is too weak to extract a sensible estimate from Fig. 5. The dispersion relation (1) also implies that the (horizontal) group velocity decreases with increasing *f*. As a consequence, it will take more time for the transients to leave the domain of interest (this will be confirmed below when we consider the development in time of available potential energy).

Frequency spectra of the total energy computed at two moorings, before and after reflection of the M2 beam, are displayed in Fig. 6. The M4 component is still excited, but with an energy level four times lower than in the non-rotating case, while the other harmonics do not emerge clearly from the spectra. This implies that energy transfer toward high frequencies is impeded by Coriolis effects. The slope of the spectra after reflection is close to -2, suggesting a superposition of randomly phased quasi-linear waves. As in the non-rotating case, we computed the ratio between total kinetic and available potential energy (Fig. 6). The numerical results are in fairly close agreement with the theoretical curve for linear waves. This suggests that the slope of the frequency spectra after reflection is consistent with the Garrett–Munk model (Munk, 1981), and also with in situ measurements near a continental slope (see, e.g., van Haren et al., 2002).

4. Analysis of mixing

4.1. Background

In what follows we will analyse the intensity of mixing in a quantitative way by employing the classical concept of available potential energy, introduced by Lorenz (1955). The key idea is to distinguish two fundamentally different ways in which the potential energy of a system can

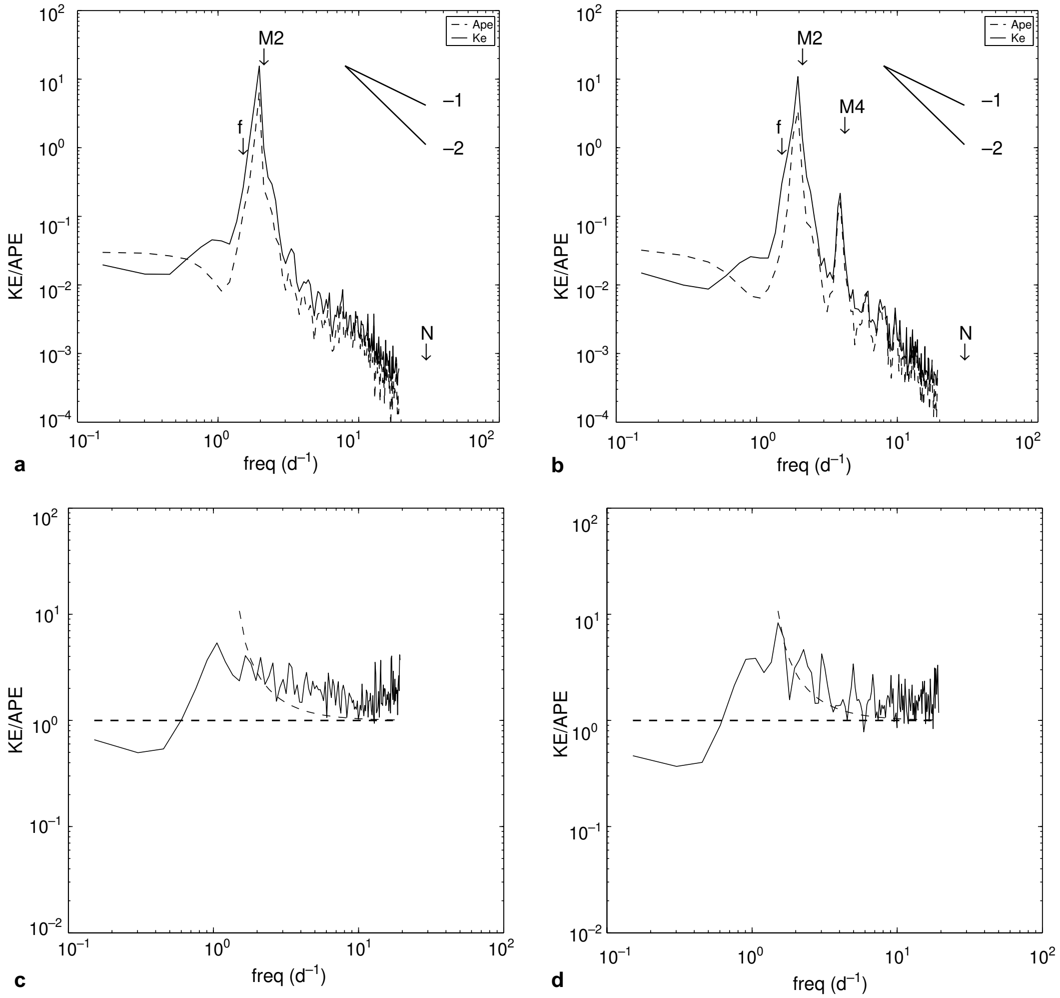

Fig. 6. Case with rotation. Frequency spectra of kinetic and available potential energy at two different "moorings", before and after reflection of the tidal beam: (a) at $x = 190$ km; (b) at $x = 168$ km; (c) ratio of total kinetic energy and available potential energy, as a function of frequency at $x = 190$ km; (d) the same ratio, but now at $x = 168$ km.

change: on the one hand by reversible processes (like the oscillatory motion in internal waves) and on the other hand by irreversible processes (like mixing). In considering a system at a certain moment, we can calculate the instantaneous potential energy E_{i}. One can 'undo' any past working of reversible processes by adiabatically re-stabilizing the vertical column. This procedure is particularly simple in a Boussinesq system, for such a system conserves volume-elements (rather than mass). Interchanging 'adiabatically' two elements of equal volume then means: interchanging them while conserving the mass of each individual element. (In a Boussinesq system, an exchange of heat is mimicked by an exchange of mass: 'supplying heat' translates to 'extracting mass', and vice versa.) By interchanging elements this way, one obtains a sorted stable column, which has a monotonic vertical temperature (and density) distribution. This sorted column then has the minimal potential energy possible under adiabatic changes: E_s. The available potential energy E_a is then given by $E_a = E_i - E_s$. Bouruet-Aubertot et al. (2001) used this method in numerical calculations on internal waves. In the present analysis, we take it one step further, into the oceanographic context.

An alternative way to obtain E_a was presented by Holliday and McIntyre (1981), in terms of an expansion that holds for general $N(z)$. For constant N only the first term of this expansion remains, giving (in terms of temperature, α being the thermal expansion coefficient):

$$E_{\mathrm{a,loc}} = \frac{g^2 \rho_* \alpha^2}{2N^2} \int \mathrm{d}x\,\mathrm{d}z (T')^2, \tag{2}$$

where T' denotes the local deviation of temperature with respect to the "undisturbed" field $T_0(z)$; ρ_* is a constant reference value of density. As we will demonstrate below, in a system in which mixing takes place, one cannot simply take the initial temperature field for $T_0(z)$.

One can apply the procedure of sorting at any given moment; one thus obtains $E_s(t)$. In a closed system where no irreversible processes take place, this quantity will be constant in time; irreversible processes can make it only larger, never smaller (an implication of the second law of thermodynamics). The system under consideration here is not closed, since it has open boundaries on the shelf and in the deep ocean. One may expect, however, that the role of these open boundaries becomes less noticeable once the transients have left the system, and if one then considers only consecutive instants having the same phase of the tide (i.e. $E_s(t_0 + nT)$, where t_0 is arbitrary, n an integer, and T the tidal period). The latter restriction means that one considers moments at which the influx is the same.

We denote the rate of increase of E_s due to irreversible mixing processes by Φ_d. Mixing locally results from a flux across iso-temperature surfaces, ϕ_d, whose volume averaged amounts to Φ_d, up to a scaling factor. We shall derive those quantities via sorting, and follow for this purpose the methods developed by Thorpe (1977), Winters et al. (1995) and Winters and D'Asaro (1996).

4.2. Case without rotation

4.2.1. Computation of the background and available potential energy

As noticed above, near the upper part of the slope, in the vicinity of the generation region, one finds small scale features; they are more clearly visible in Fig. 8a, an unsmoothed enlargement of Fig. 2b. These small-scale processes suggest that mixing takes place. In reality, mixing occurs at scales not resolved by the model; however, the relatively large values of diffusivity as well as the working of the KPP-scheme enable us to mimick the process of mixing at a larger scale.

This idea is confirmed in Fig. 7, where we have chosen $t_0 = 0$. In these figures we show the total potential energy of the entire xz-domain (i.e. the energy density is integrated over the xz-region, hence the resulting unit J m^{-1}); we present it in normalized form by setting the initial value $E_i(0)$ equal to zero. Fig. 7a shows the instantaneous potential energy E_i and the sorted E_s; Fig. 7b shows their difference: the available potential energy E_a. One observes a steady increase in both E_i and E_s (Fig. 7a); the steady increase in the sorted potential energy E_s is due to the ongoing irreversible processes (mixing). The available potential energy, on the other hand, becomes nearly constant during the last four tidal periods (Fig. 7b) implying that most of the transients have left the domain by that time. The local expression (2) yields values that are too large; here we used the

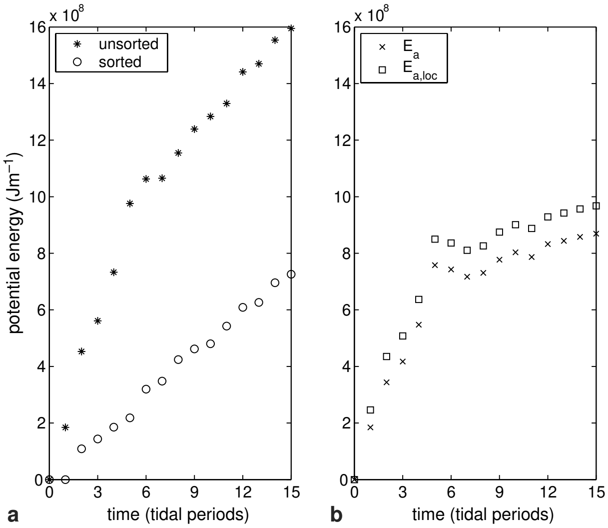

Fig. 7. Development in time of the potential energy, integrated over the entire *xz*-domain, and then normalized: (a) The instantaneous unsorted potential energy E_i (asterisks), and the sorted potential energy E_s (circles). (b) Their difference, the available potential energy $E_a = E_i - E_s$ (crosses); the potential energy calculated from the local expression (2) in squares.

initial temperature field as the "undisturbed" field. The difference between the two arises in the first few periods and remains nearly constant afterwards, which suggests that the difference is due to adjustment of the system to the forcing, which involves net changes in mass.

4.2.2. Computation of the Cox number

Mixing may be quantified by a turbulent diffusivity. Consistently with the concepts introduced above, the turbulent diffusivity should be defined as (Winters and D'Asaro, 1996):

$$\kappa_s = -\frac{\phi_d}{dT_s/dz}, \tag{3}$$

where T_s is the sorted temperature profile (and ϕ_d is the thermal flux). When the flow is homogeneous along the horizontal direction, the fluid system to which the sorting method is applied may consist of the whole fluid volume. If, moreover, N is constant, a volume averaged value can be defined for the turbulent diffusivity, which is proportional to Φ_d (the production of background potential energy through mixing) divided by the vertical gradient of the sorted temperature profile. In the present case, N is constant but the flow is not homogeneous along the horizontal direction so that we apply the sorting method to fluid columns, following Thorpe (1977). A method to conveniently obtain the diapycnal flux, and hence the turbulent diffusivity, was proposed by Winters and D'Asaro (1996). The first step in this method is to sort the temperature profile, along with its gradient (i.e. the gradient is not sorted itself but is simply re-arranged following the sorting of the profile). The sorted profile is denoted by T_s, and the correspondingly re-arranged gradient by $[\nabla T]_s$. The ratio between $[\nabla T]_s^2$ and $(dT_s/dz)^2$ directly provides the normalized turbulent diffusivity:

$$\left(\frac{[\nabla T]_{\mathrm{s}}}{\mathrm{d}T_{\mathrm{s}}/\mathrm{d}z}\right)^{2}=\frac{\kappa_{\mathrm{s}}}{\kappa}\equiv \mathrm{Cox}, \tag{4}$$

where “Cox” refers to the Cox number (note that $[\nabla T]_{\mathrm{s}}$ may often be computed as $[\mathrm{d}T/\mathrm{d}z]_{\mathrm{s}}$, to a good approximation, as we did). We note that “κ”, in the denominator of the second ratio is the background diffusivity. The spatial distribution of the Cox number over the slope is shown in Fig. 8b; for comparison, the temperature perturbations are shown in Fig. 8a. Both are taken after 15 tidal periods. Because the Cox number varies significantly on the grid scale, we took horizontal averages over every 10 points, thus creating segments of 5 km length. This length was chosen because it is of the order of the width of the beam. In general, the large values of the (horizontally averaged) Cox number are located over the upper part of the slope, and locally in the beam (clearly visible in the deeper parts of the basin, between $x = 200$–250 km). Examples of three vertical distributions are shown in Fig. 9; over the upper part of the slope, values as high as 20 are reached, implying that the effective diffusivity is 20κ. Note that similar values of the Cox number were obtained by Bouruet-Aubertot et al. (2001) for breaking internal gravity waves in a two-dimensional vertical plane.

4.2.3. Dependence on background diffusivity

We now consider whether the Cox number depends significantly on the value of the background diffusivity (i.e. the constant vertical diffusivity). For this purpose, we did two additional calculations, in all respects equal to the previous one except that we took vertical diffusivity equal to 10^{-3} m^2/s (and vertical viscosity, too) in one case, an increase with respect to the previous run, and equal to 10^{-5} m^2/s in another. The results are shown in Fig. 10. Overall, the magnitude of the values does not change strongly, but the region of higher Cox number becomes larger as the background diffusivity becomes smaller.

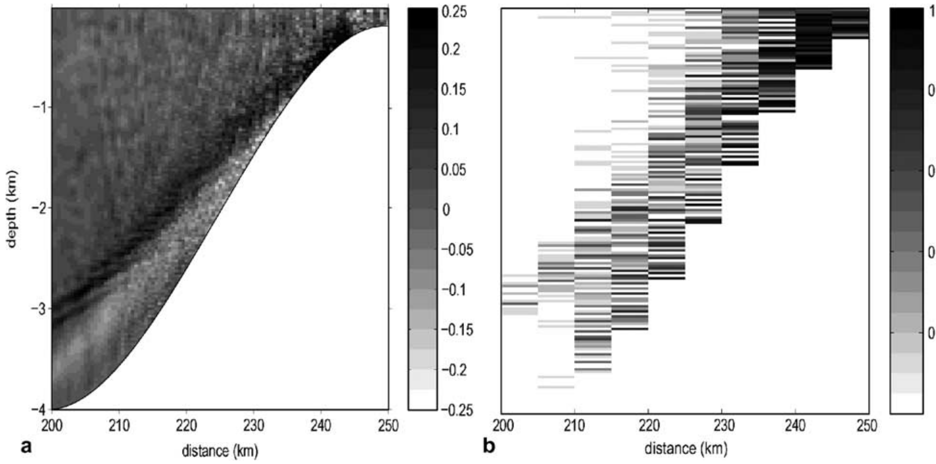

Fig. 8. (a) The temperature field (in °C) over the slope, after 15 tidal periods, with the initial (static) temperature field subtracted. (b) The distribution of the Cox number over the slope, where averages were taken over every 10 points, in the horizontal. Note that the logarithm (base 10) of the Cox number is plotted.

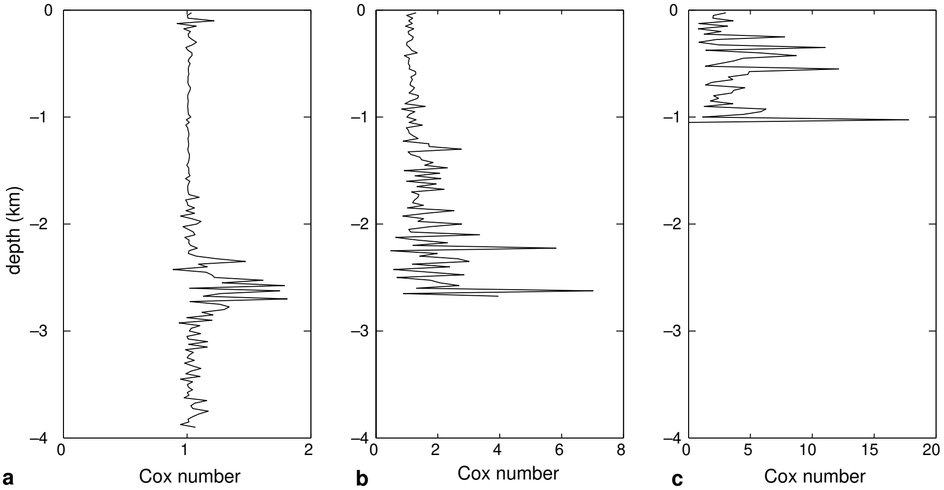

Fig. 9. Vertical distributions of Cox numbers over the slope, after 15 tidal periods. Averages were taken over every 10 points. (a) Average between 205 and 210 km; (b) between 220 and 225 km; (b) between 235 and 240 km. Notice the different scaling along the horizontal axis.

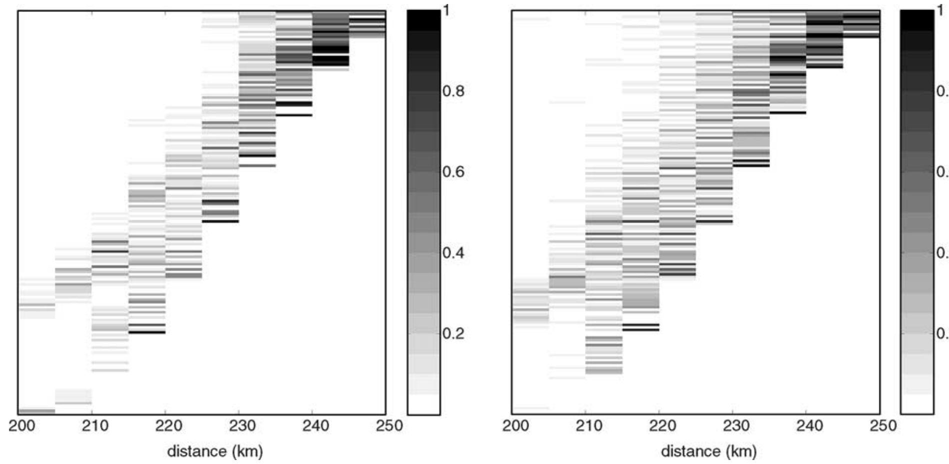

Fig. 10. Results plotted as in Fig. 8b, but now for higher and lower vertical background diffusivity (10^{-3} m^2/s in the left-hand panel; 10^{-5} m^2/s in the right-hand panel).

4.3. Case with rotation

As noted above, the group velocity decreases due to Coriolis effects; hence it takes longer for the transients to leave the domain. This is confirmed in Fig. 11b where we see that the available potential energy still increases markedly even after 12 tidal periods, near the end of the calculation (cf. Fig. 7b). Typically, one finds that some 40 or 50 tidal periods would be needed for the internal-tide signal to become fully “stationary” in the presence of Coriolis effects (Gerkema

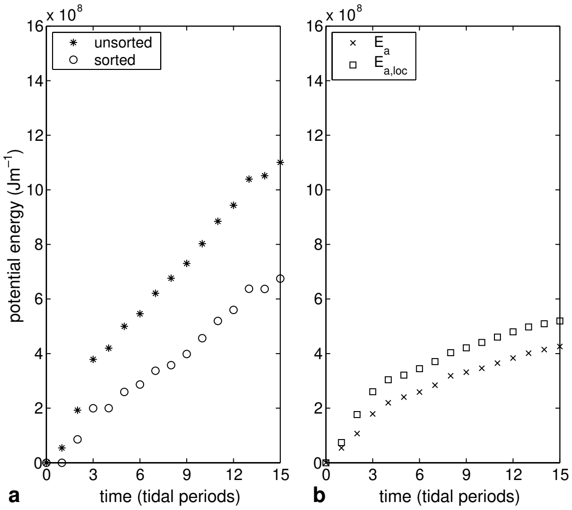

Fig. 11. Case with rotation. Development in time of the potential energy, integrated over the entire *xz*-domain, and then normalized: (a) the instantaneous unsorted potential energy E_i (asterisks), and the sorted potential energy E_s (circles), (b) their difference, the available potential energy $E_\mathrm{a} = E_\mathrm{i} - E_\mathrm{s}$ (crosses); the potential energy calculated from the local expression (2) in squares.

et al., 2004); this depends of course also on the vertical resolution, i.e. on how many vertical modes are resolved.

The potential energy, in all its forms, is lower than in the case without rotation. This is partly because the equipartition between kinetic and potential energy no longer holds in the presence of rotation.

The Cox numbers (not shown) are generally smaller than in the case without rotation, by about a factor 2. This confirms the idea noticed above (with regard to the weaker higher harmonics) that in the presence of rotation non-linear effects are less manifest.

5. Discussion

The results presented in this paper show that there are essentially two regions where non-linear effects manifest themselves: over the upper part of the slope (the generation region), and at the position where the beam first reflects (bottom).

In the former region, small-scale features are found, suggestive of breaking and mixing. We have analysed this quantitatively by calculating the development of changes in the potential energy due to irreversible processes, and the values of the Cox number over the slope.

In the latter region, higher harmonics are created. Our analysis indicates that about half of the loss of energy of the M2 beam, during its reflection, is due to dissipation, while the other half goes into the transfer to higher frequencies. The presence of higher harmonics seems to be confirmed by observations. For example, year-long observations in the Central Bay of Biscay reveal distinct peaks of the higher harmonics in internal-wave spectra (van Haren, 2003). Detailed observations on internal-tide beams are scarce, but the results obtained by Pingree and New (1991) provide some insight into the structure of the beam over the vertical. Just beyond the position of bottom reflection, they find a nearly sinusoidal M2 signal in the lowest part of the watercolumn, while higher up in the column the signal becomes increasingly non-sinusoidal (their Fig. 5). This would be consistent with the passage of higher harmonics (and hence steeper) internal-tide beams at higher positions, since the superposition of M2 and its higher harmonics would produce a non-sinusoidal signal.

The generation of higher harmonics upon bottom reflection of internal-tide beams seems to be a fairly generic phenomenon; for example, it was also observed in a different type of configuration, namely over a deep seamount (Lamb, 2004), instead of a continental slope. The intensity of the beam has of course to be sufficient for several harmonics to be created. In the non-rotating laboratory experiments by Peacock and Tabaei (2005) of a wave beam reflecting on a sloping boundary, a single harmonic is generated.

We found that Coriolis effects partly suppress the transfer of energy to higher harmonics. The theoretical framework required to explain the suppression is still lacking. Thorpe (1987) considered reflecting internal waves with Coriolis effects, but he found that no higher harmonics are generated upon reflection at a *flat* bottom. This does not contradict our findings, because he considered incoming waves of the form $\exp ik\xi$ (with ξ the characteristic coordinate), a wave of infinite transverse extension, whereas we consider an internal-wave *beam*. The case of a reflecting beam was recently studied by Tabaei et al. (2005), but without Coriolis effects. An extension of this work should shed light on the latitudinal dependence.

We note that suppression, due to Coriolis effects, of a transfer to higher frequencies is found in other contexts, too. For example, it was found by Gerkema and Zimmerman (1995) that the transfer from internal tides to interfacial solitary waves was impeded by Coriolis dispersion. In yet another context, inhibition of energy transfer by Coriolis effects has been studied in a theoretical and numerical analysis by Cambon et al. (1997) for a rotating turbulent flow, without stratification.

Notice that by varying the Coriolis parameter (f) one changes a number of things at once, such as the conversion rate (not discussed in this paper) and thereby the energetics of the beam, the direction of the beam, as well as its width. There are, therefore, various ways in which one can make a comparison, and it is not clear which is the most meaningful one. We kept all other parameters the same, but one may also consider varying, for instance, the barotropic flux along with the Coriolis parameter in order to keep the conversion rate fixed. Similar ambiguities arise if one changes N or the topographic slope.

In the numerical calculations, the available potential energy gradually grows with time until it reaches a nearly steady value; this takes between 12 and 15 tidal periods for the domain we considered here. The reason is that it takes a relatively long time for the higher modes to reach the boundaries of the domain, because of their lower group speeds. This is seen in very short runs, which produce only a first mode at some distance from the generation region (see, e.g., Legg, 2004). The above results show that one does find a well-defined beam (as well as narrow beams of higher harmonics after reflection) if the run is sufficiently long; the beam, of course, results from a superposition of a number of modes. This highlights the necessity of taking a long time span; otherwise one basically looks only at the transient response.

The results presented here can be regarded as a reasonable idealization of the state during winter, when the stratification varies only weakly. The presence of the seasonal thermocline (summer) would give rise to a more complicated picture, because it would create an additional region of strong forcing (in the thermocline), and moreover would give rise to scattering of internal tide beams (Gerkema et al., 2004).

It should be noticed that the horizontal resolution was still fairly coarse in the present calculations. This implies, among other things, that non-hydrostatic effects are diminished; they would be more pronounced with a finer resolution. Specifically, the inclusion of a seasonal thermocline, as a next step, would require a finer resolution to resolve the formation of solitary waves, which depend crucially on non-hydrostatic effects.

Acknowledgments

We thank Aunick Pichon and EPSHOM for supporting this work, under contract CA2003/01/CMO. We are grateful to the assistance received from IDRIS, the french national computer center, on whose computers the calculations were performed (contracts 030580 and 040580); and to the MIT-gem team for helpful suggestions that enabled us to get the model working.

References

Baines, P.G., 1982. On internal tide generation models. Deep-Sea Res. 29 (3A), 307–338.

Bouruet-Aubertot, P., Sommeria, J., Staquet, C., 1996. Stratified turbulence produced by internal wave breaking: two-dimensional numerical experiments. Dynam. Atmos. Oceans 23, 371–378.

Bouruet-Aubertot, P., Koudella, C., Staquet, C., Winters, K.B., 2001. Particle dispersion and mixing induced by breaking internal gravity waves. Dynam. Atmos. Oceans 33, 95–134.

Cambon, C., Mansour, N.N., Godeferd, F.S., 1997. Energy transfer in rotating turbulence. J. Fluid Mech. 337, 303–332.

Gerkema, T., 2002. Application of an internal-tide generation model to baroclinic spring-neap cycles. J. Geophys. Res. 107 (C9), 3124. doi:10.1029/2001JC001177.

Gerkema, T., Zimmerman, J.T.F., 1995. Generation of nonlinear internal tides and solitary waves. J. Phys. Oceanogr. 25 (6), 1081–1094.

Gerkema, T., Lam, F.P.A., Maas, L.R.M., 2004. Internal tides in the Bay of Biscay: conversion rates and seasonal effects. Deep-Sea Res. II 51 (25/26), 2995–3008.

Holliday, D., McIntyre, M.E., 1981. On potential energy density in an incompressible, stratified fluid. J. Fluid Mech. 107, 221–225.

Jézéquel, N., Mazé, R., Pichon, A., 2002. Interaction of semidiurnal tide with a continental slope in a continuously stratified ocean. Deep-Sea Res. I 49, 707–734.

Khatiwala, S., 2003. Generation of internal tides in an ocean of finite depth: analytical and numerical calculations. Deep-Sea Res. I 50, 3–21.

Lamb, K.G., 2004. Nonlinear interaction among internal wave beams generated by tidal flow over supercritical topography. Geophys. Res. Lett. 31, L09313. doi:10.1029/2003GL019393.

Large, W.C., McWilliams, J.C., Doney, S.C., 1994. Oceanic vertical mixing: a review and a model with a nonlocal boundary layer parametrization. Rev. Geophys. 32 (4), 363–403.

Legg, S., 2004. Internal tides generated on a corrugated continental slope. Part I: Cross-slope barotropic forcing. J. Phys Oceanogr. 34, 156–173.

LeBlond, P.H., Mysak, L.A., 1978. Waves in the Ocean. Elsevier.

Lien, R.-C., Gregg, M.C., 2001. Observations of turbulence in a tidal beam and across a coastal ridge. J. Geophys Res. 106, 4575–4592.

Lorenz, E.N., 1955. Available potential energy and the maintenance of the general circulation. Tellus 7, 157–167.

Marshall, J., Adcroft, A., Hill, C., Perelman, L., Heisey, C., 1997. A finite-volume, incompressible Navier–Stokes model for studies of the ocean on parallel computers. J. Geophys. Res. 102 (C3), 5753–5766.

Mowbray, D.E., Rarity, B.S.H., 1967. A theoretical and experimental investigation of the phase configuration of internal waves of small amplitude in a density stratified liquid. J. Fluid Mech. 28, 1–16.

Munk, W., 1981. Internal waves and small-scale processes. In: Warren, B.A., Wunsch, C. (Eds.), Evolution of Physical Oceanography. MIT Press, pp. 264–291.

Peacock, T., Tabaei, A., 2005. Visualization of nonlinear effects in reflecting internal wave beams. Phys. Fluids 17, 061702.

Pingree, R.D., New, A.L., 1991. Abyssal penetration and bottom reflection of internal tidal energy in the Bay of Biscay. J. Phys. Oceanogr. 21 (1), 28–39.

Tabaei, A., Akylas, T.R., 2003. Nonlinear internal gravity wave beams. J. Fluid Mech. 482, 141–161.

Tabaei, A., Akylas, T.R., Lamb, K.G., 2005. Nonlinear effects in reflecting and colliding internal wave beams. J. Fluid Mech. 526, 217–243.

Thorpe, S.A., 1977. Turbulence and mixing in a Scottish Loch. Phil. Trans. R. Soc. Lond. A286, 125–181.

Thorpe, S.A., 1987. On the reflection of a train of finite-amplitude internal waves from a uniform slope. J. Fluid Mech. 178, 279–302.

Turner, J.S., 1973. Buoyancy Effects in Fluids. Cambridge University Press.

van Haren, H., 2003. On the polarization of oscillatory currents in the Bay of Biscay. J. Geophys. Res. 108 (C9), 3290. doi:10.1029/2002JC001736.

van Haren, H., Maas, L.R.M., van Aken, H., 2002. On the nature of internal wave spectra near a continental slope. Geophys. Res. Lett. 29 (12), 1615. doi:10.1029/2001GL014341.

Winters, K.B., D'Asaro, E.A., 1996. Diascalar flux and the rate of fluid mixing. J. Fluid Mech. 317, 179–193.

Winters, K.B., Lombard, P.N., Riley, J.J., D'Asaro, E.A., 1995. Available potential energy and mixing in density-stratified fluids. J. Fluid Mech. 289, 115–128.